

Defect Interaction and Deformation in Graphene

Wei Zhang^{a,b}, *Minsung Kim*^b, *Rong Cheng*^{b,c}, *Wen-Cai Lu*^{a,c}, *Hong-Xing Zhang*^a, *K. M. Ho*^b, *C. Z. Wang*^{b*}

^a International Joint Research Laboratory of Nano-Micro Architecture Chemistry and Institute of Theoretical Chemistry, Jilin University, Changchun, Jilin 130023, People's Republic of China

^b Ames Laboratory-U.S. DOE and Department of Physics and Astronomy, Iowa State University, Ames, Iowa 50011, USA

^c College of Physics and State Key Laboratory of Bio-Fibers and Eco-Textiles, Qingdao University, Qingdao, Shandong 266071, China

ABSTRACT:

Interactions between defects in graphene and the lattice distortion and electronic charge localization induced by the defect interactions are studied by tight-binding (TB) calculations using the recently developed three-center TB potential model. The interaction between two 5-7 Stone-Wales defects gliding along the zig-zag direction of the graphene, which has been observed by experiment, is studied at first to validate the TB calculations. Reconstructed divacancy defect pairs and di-atom defect pairs separated along the glide zigzag (ZZ) and armchair (AC) directions in graphene respectively are then studied. We show that the characteristic (i.e., attractive or repulsive) and the strength of interactions between these defects are dependent on the type of defects and on the direction and distance of the defect separation on graphene. While elastic interaction due to the graphene lattice distortion induced by the defect has significant contribution to the total interaction energy, redistribution of electron charges caused by the defects also plays an important role in the defect-defect interaction.

KEYWORDS: Tight-binding calculation; Defects in graphene; First-principles calculations; Formation energy

1. INTRODUCTION

Ideal graphene is often represented as a flat membrane with virtually no defects. In reality, its surface is easily affected by deformation due to the material's elasticity influence in the third dimension, which gives rise to strained structures such as ripples and bubbles.¹⁻⁸ In addition to physical deformation, the carbon atoms of graphene can also be removed, added or rearranged during growth⁹⁻¹¹ and defects are introduced into the material. Recent experimental studies show that various defects can be introduced into graphene using focused electron beam irradiations.¹²⁻¹⁶ These defects inevitably affect the physical properties of graphene.^{17, 18}

Many theoretical studies indicate that the presence of defects or strained structures in graphene can alter its electronic as well as chemical properties.¹⁹⁻²¹ The structure of graphene provides unusual mechanical^{22, 23} and electronic properties,²⁴ which can be influenced by point defects and dislocations.^{25, 26} Point defects and dislocations can lead to spin polarization and magnetism in graphene that would be important for extending graphene's electronic applications into spin-based technology.^{27, 28} Understanding how defects interact with each other and how defects deform graphene helps build an accurate description of both elasticity and plasticity in graphene.²⁹⁻³¹ Studying the interaction between defects and how to the strain fields respond are also

very important for developing complete structural models of graphene. Although the movement and interaction of defects and their effect on the mechanical and electronic properties of materials have been massively studied,^{32, 33} the defect structures on graphene studied so far mainly have been based on the 57 pairs. The research showed the long range strain fields favor gliding of 57 dislocation cores in opposite directions, while the local curvature energy of two oppositely directed 57 pairs is minimized when they are adjacent and form a SW point defect.^{14, 32, 33} The glide of 57 pairs can also be facilitated by the formation of chains of dislocation dipoles, which effectively screen stress fields of the separated 57 pairs.^{14, 32} The details of the movement of defect pairs are still not fully understood due to the prior technical limitations of experiments. Studies that provide a detailed understanding of the process of defect interaction and movement will help make it possible to control dislocations in the future.

In this paper, we provide insight into the mechanisms by which defects lead to dislocation pairs in graphene which directly affect the structural and electronic properties of graphene. We first study the interaction between a 57 pair in graphene which has been observed in experiment¹⁴ and compare our TB calculations with first-principles calculations to validate our calculation model. Then by including to two reconstructed divacancy defects and two-atom defects along the glide zigzag (ZZ) direction and armchair (AC) on graphene respectively, we study the nature of the interaction between the two defects, i.e., repulsive or attractive, as well as the lattice deformation and electron redistribution induced by the defect interactions. The results from our calculations can help further clarify the formation process of dislocations on

graphene.

The rest of the paper is arranged as follows. In section 2, we describe the structure models and calculation methods used in the paper. In the Results and Discussions section (section 3) we first present the results for the interaction between a 57 pair on graphene to validate our calculation methods in comparison with first-principles calculations and available experiment. Then the calculation results on the interaction between a reconstructed divacancy pair and that between a two-atom pair will be presented and the origin of the attractive or repulsive interaction will be discussed. Finally, conclusions are given in section 4.

2. CALCULATION METHODS

Most of the calculations in this paper use the three-center tight-binding model developed recently by us.³⁴ Some first-principles calculations with smaller unit cell are also performed to help understand the TB results. The interatomic interactions in TB method are based on quantum mechanical descriptions thus have better accuracy than those from empirical classical potential. At the same time, it can provide faster computing speed than DFT method because it used minimal basis and the hopping and overlap integrals are parametrized. Our three-center tight-binding potential model for carbon has been demonstrated to exhibit excellent accuracy and transferability.³⁴ It describes well the band structures, binding energies and other properties of various carbon crystalline structures and surfaces as well as the structures and energies of various isolated point defects on graphene.^{35,36} The readers are referred to Refs 34-36

for more detail descriptions of our three-center TB model for carbon.

The first-principles density functional theory (DFT) calculations were performed using Vienna Ab-initio Simulation Package (VASP).^{37, 38} Projector-augmented wave (PAW)³⁹ and Perdew-Burke-Ernzerhof (PBE) exchange-correlation functional⁴⁰ were used in the calculations. We employed plane-wave basis set with 400 eV energy cutoff.

For studying the interaction between a 57 pair on graphene, we take the structure model from the experimental observation.¹⁴ The 57 pair is separated along the zig-zag direction by 1-6 steps with 0-5 hexagon rings between the two defects. The defect structures in a supercell of 224 carbon atoms are calculated by both TB and DFT for comparison in order to validate the accuracy of the TB model for describing the interaction between the defects. Large supercell contain 896 atoms is also calculated to evaluate the effects of elastic relaxation of the interaction energy of the defects.

For studying the interactions between a pair of reconstructed divacancy defects or two-adatom defects, three structural models are used. The first model is a 32×32 graphene lattice containing two divacancy (V_2) defects of 555-777 reconstructed configurations. The number of atoms in this supercell is 2044. The second and third models consist of a pair of two-adatom (A_2) defects in the 7-55-7 reconstructed configuration in a 32×32 graphene supercell. The two A_2 defects can be on the same side (model 2) or different sides of graphene (model 3). The number of atoms in these two models is 2052. The atomic structures near the defects in the supercell are shown in Fig. 1. The $V_2(555-777)$ is the energetically most favorable structure for a V_2 vacancy which has three five-membered and three seven-membered rings as shown in Fig. 1.

The most stable structure for embedding two atoms (A_2) is also shown in Fig. 1 which is composed of a pair of joined pentagonal carbon rings placed between a pair of heptagonal rings, i.e., a $A_2(7-55-7)$ structure. Thus we only consider the $V_2(555-777)$ and $A_2(7-55-7)$ configurations here as dislocation pairs separated along the Zig-Zag and Armchair glide directions on pristine graphene, respectively. These structure models are based on the most stable reconstructed structures of divacancy and A_2 embedded atoms in graphene obtained from our TB calculations.^{35,41}

Periodic boundary conditions are used with a vacuum region of 50\AA in the direction perpendicular to the graphene. The defect structures at given separation distances are relaxed to local minimums until the forces on every atom are less than 0.01 eV/\AA . The formation energies, E_f , of the defect complexes were calculated using the equation,

$$E_f = E_T - N\mu, \quad (1)$$

where E_T is the total energy of the defected graphene and μ is the chemical potential of a carbon atom in perfect graphene. N is the number of carbon atoms in the supercell.

3. Results and Discussions

3.1 Interaction Between a 57 Pair: Validation of TB Calculations. Fig. 2 shows the formation energy of a 57 pair defect on graphene as the function of the separation between the pair from the TB and DFT calculations. The separation is denoted by gliding step 1-6 (i.e., 0-5 carbon hexagons) between them. It can be seen that the formation energy is the lowest when the two 57s are adjacent (step-1). The formation

increases as the separation distance between the defect pair increases, indicating that

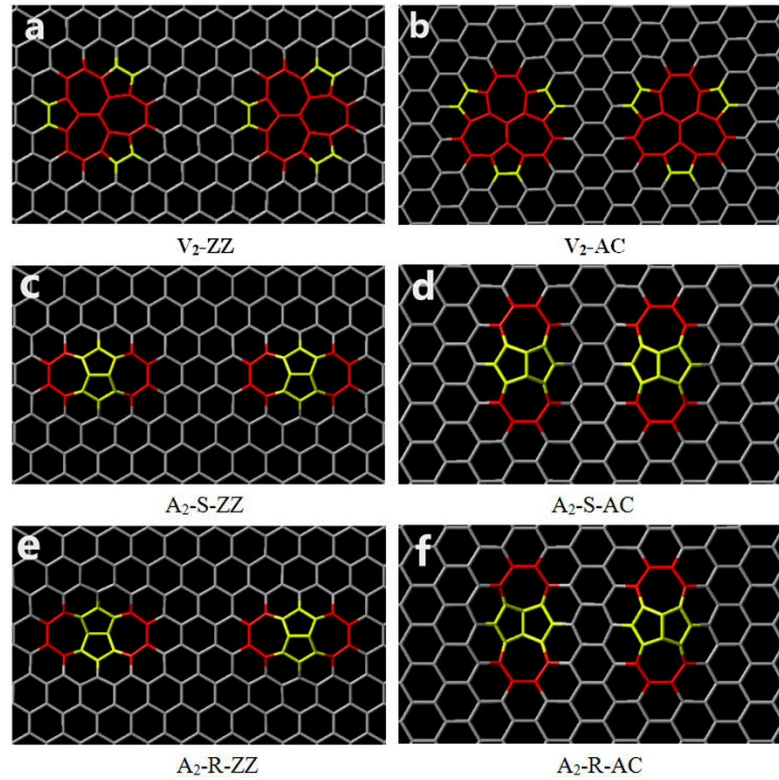


Figure 1. Structure models used in the present study. (a) Two reconstructed 555-777 divacancy defects along the zigzag direction in graphene (V_2 -ZZ); (b) Two reconstructed 555-777 divacancy defects along the armchair direction in graphene (V_2 -AC); (c) Two reconstructed 7-55-7 two-adatom defects along the zigzag direction on the same side of graphene (A_2 -S-ZZ); (d) Two reconstructed 7-55-7 two-adatom defects along the armchair direction on the same side of graphene (A_2 -S-AC); (e) Two reconstructed 7-55-7 two-adatom defects along the zigzag direction on the reverse sides of graphene (A_2 -R-ZZ); (f) Two reconstructed 7-55-7 two-adatom defects along the armchair direction on the reverse sides of graphene (A_2 -R-AC).

the 57 defects are strongly attractive. The behavior observed from the theoretical calculations are consistent with the observations from the experiment of Ref. 14.

Moreover, it can be seen from the figure that the results of the formation energy for the supercell of 224 atoms from the TB calculations are very close to those from first principles calculations at the same size. This comparison indicate that TB calculations have the adequate accuracy in describing the defects interactions in graphene. With the

computational efficiency and accuracy, TB calculations can handle larger supercell calculation to properly deal with possible longer range elastic relaxation effects so that inclusion of *ad hoc* corrections¹⁴ are not necessary. As one can see from Fig. 2, calculations using larger supercell (896 atoms) lower the formation energies in comparison with those from 224-atom supercell, because the strain induced by the defects can be more fully relaxed in larger supercell. The effects of elastic relaxation become more significant when the separation between the 57 defects become larger (i.e., with separation more than 3 steps) as one can see from Fig. 2. The energy correction due to strain interaction at step 6 is about 4 eV which is consistent with that reported in Ref. 14.

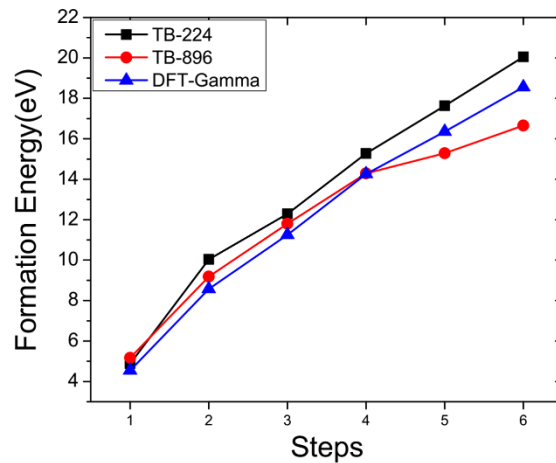


Figure 2. Formation energy of the 57 pair on graphene as the function of the separation distance (in terms of gliding step) from TB and first-principles DFT calculations.

The comparison of carbon-carbon bond length deviation with respect to that of perfect graphene (1.42 Å) induced by the presence of the 57 pair from the DFT and TB calculations is shown in Fig. 3. One can see that the bond length distortion induced by

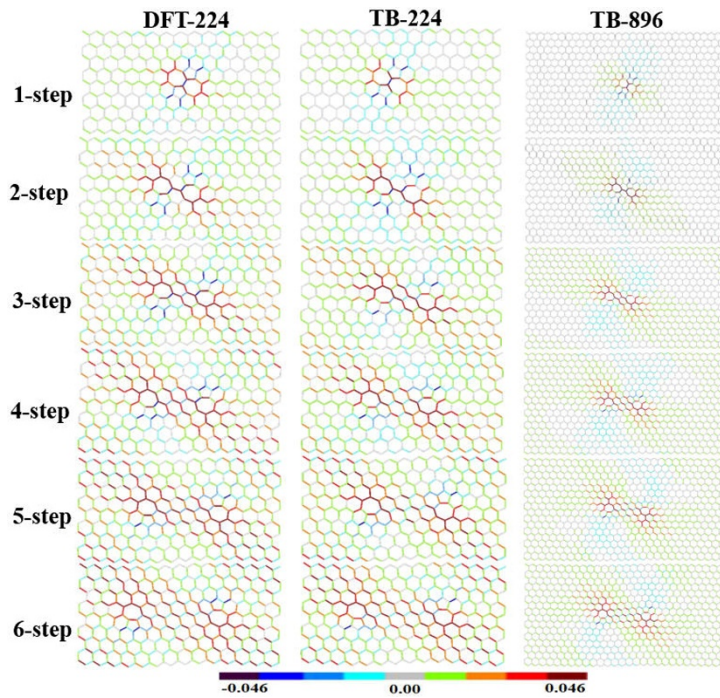


Figure 3. Comparison of carbon-carbon bond length deviation from that of perfect graphene (1.42 \AA) induced by the presence of the 57 pair from the DFT and TB calculations. The deviation amplitudes are indicated by the color bar in the unit of \AA .

the 57 pair is propagated along the arm-chair (AC) directions although the 57 pair is separated along the zig-zag direction. It is also interesting to note that the bond length is stretched (red) in one AC direction while compressed (blue) in another AC direction 120 degree apart. We also note that in the small supercell (224 atoms) calculation, noticeable bond length distortions already reach the supercell boundary for 57 pair separation of more than 2-step, indicating that effects of strain relaxation can't be well taken into account in the small cell calculation. Our calculation also indicate that a supercell of 896 atoms is sufficient for studying the interaction between the 57 pair up to the separation of 6-steps, as one can see from the right column in Fig. 3 where the strain distribution in the supercell of 896 atoms from the TB calculations are presented. Finally, we would like to point it out that the lattice distortion caused by the defects obtained from our TB calculation are very similar to that from the DFT calculation at

the same supercell size of 224 atoms. The distortions from the DFT calculations are slightly large. This similarity can also be seen from Fig. 4 where the bond lengths of the 57 pair from TB and DFT calculations using the 224-atom supercell are compared. The excellent agreement between the TB and DFT calculation in both energies and lattice distortion patterns indicate that the TB calculations are accurate and reliable.

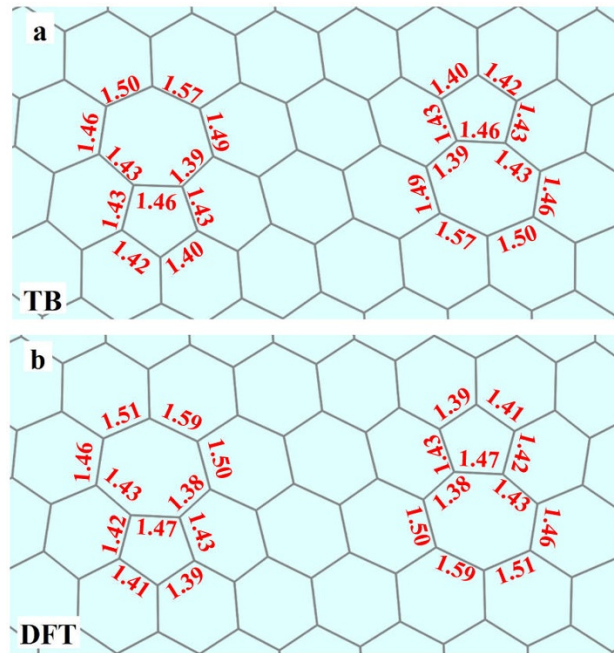


Figure 4. Comparison of bond lengths of the 57 pair by (a) TB and (b) DFT calculations. The bond lengths are in the unit of Å.

3.2 Interaction between the V_2 and A_2 defects: Attraction or repulsion. In order to gain the insights into the nature of the interactions between the V_2 and A_2 defect pairs, we calculated the formation energy, lattice distortions and electron charge redistribution of the three models as the function of the separation distances between the two defects along the zig-zag and armchair directions.

3.2.1. Interaction energies. The formation energies as the function of the separation distance d between the two defects along the zig-zag or armchair directions

in the three models are shown in Fig. 5. The black dots and red dots represent the formation energy along the ZZ direction and the AC direction, respectively. At large separation distance where the interaction between the two defects is negligible, the formation energy should be equal to the twice of the formation energy of the isolated defect which is 6.88 eV for a $V_2(555-777)$ defect and 6.31 eV for a $A_2(7-55-7)$ defect

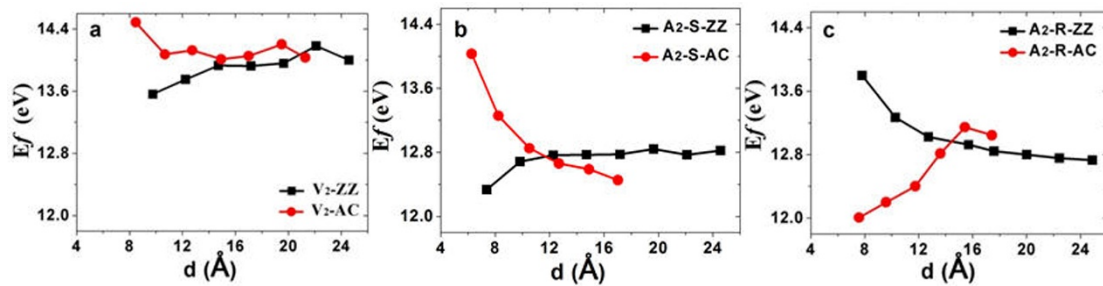


Figure 5. Formation energies of the defect complexes as the function of the defect separation distance d along the ZZ and AC directions respectively.

respectively from our previous calculations.³⁶ Although there is some noises in the calculation results, from Fig. 5 (a) we can see that two $V_2(555-777)$ defects prefer to stay along the ZZ direction and the interaction between the defects is attractive. While the two defects along the AC direction are repulsive. The same trends are the same for the case of A_2 -S complex as one can see from Fig. 5 (b). The attraction energies along the ZZ in the A_2 -S complex is also about 0.4 eV at ~ 7.4 Å, but repulsion is stronger along the AC direction. It is interesting to note that the trend of defect-defect interaction in the A_2 -R model (i.e., two A_2 defects on different sides of graphene) is opposite to that of the above two models. The two A_2 -R defects along AC direction exhibit about 1.0 eV attraction while have about 1.0 eV repulsion along the ZZ direction respectively at the separation distance of ~ 8 Å as shown in Fig. 5 (c).

3.2.2 Lattice distortion induced by the defects in graphene. To further understanding the nature of the interactions of the two defects in graphene, we have studied the lattice distortions caused by the defect pairs. The distortion patterns

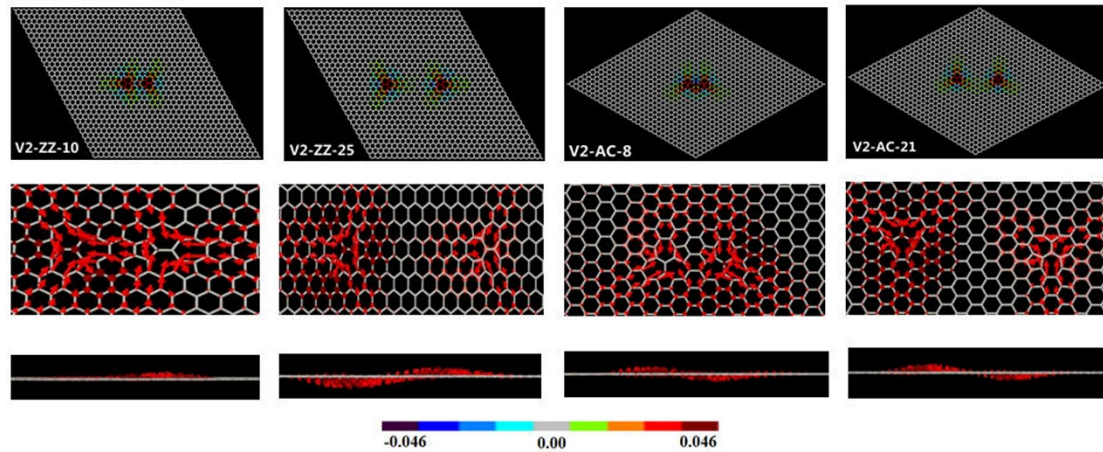


Figure 6. The interatomic bonds coloured with stretched (red) or compressed (blue) and the displacements of the carbon atoms with red arrows of the two 555-777 pair (V_2) along the glide ZZ and AC direction, respectively, according to the bond length distortion with respect to that of perfect graphene (1.42 \AA) induced by the defects pairs at different separation distances.

for the 3 types of defect pairs are shown in Figs. 6-8 respectively. On the top panel of each figure, we show the bond length variations with respect to the equilibrium bond length of perfect graphene (1.42 \AA) induced by the defect pairs at different separation distances. We see that the bond length can be stretched (red) or compressed (blue) but the distortions are very much localized around the defects. To see more details of lattice distortions induced by the defects, we also plot the displacements of the carbon atoms induced by the defect pairs along the glide ZZ and AC direction, respectively, as shown in the middle panel (top view) and lower panel (side view) of Figs. 6-8 respectively. We found the closer the distance between two dislocation pairs the deformation is larger. More details about the lattice distortions induced by the defects can also be found in

Fig. 9 and Table 1 where the sum of square of deviation in bond length and relative bond angles are presented.

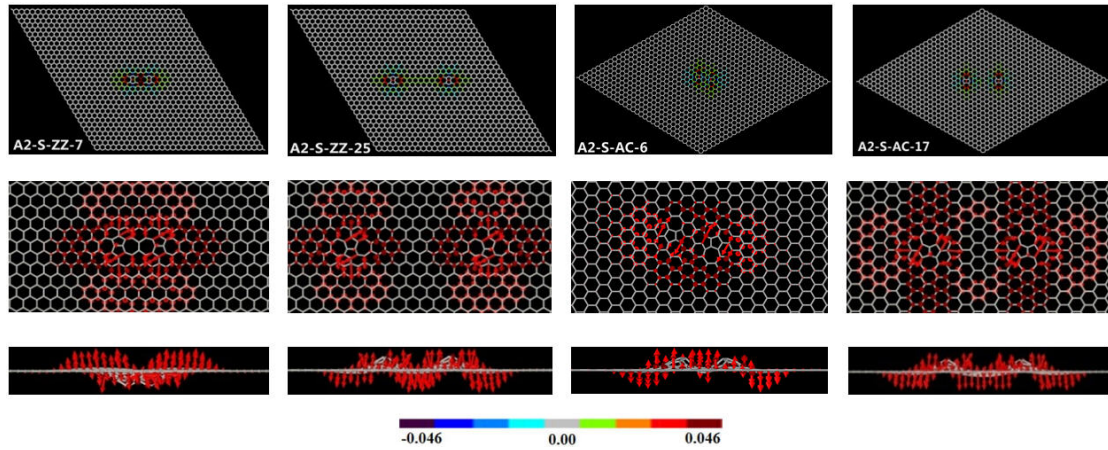


Figure 7. The interatomic bonds coloured with stretched (red) or compressed (blue) and the displacements of the carbon atoms with red arrows of the two 7-55-7 pair (A_2) defects sites are same side along the glide ZZ and AC direction, respectively, according to the bond length distortion with respect to that of perfect graphene (1.42 \AA) induced by the defects pairs at different separation distances.

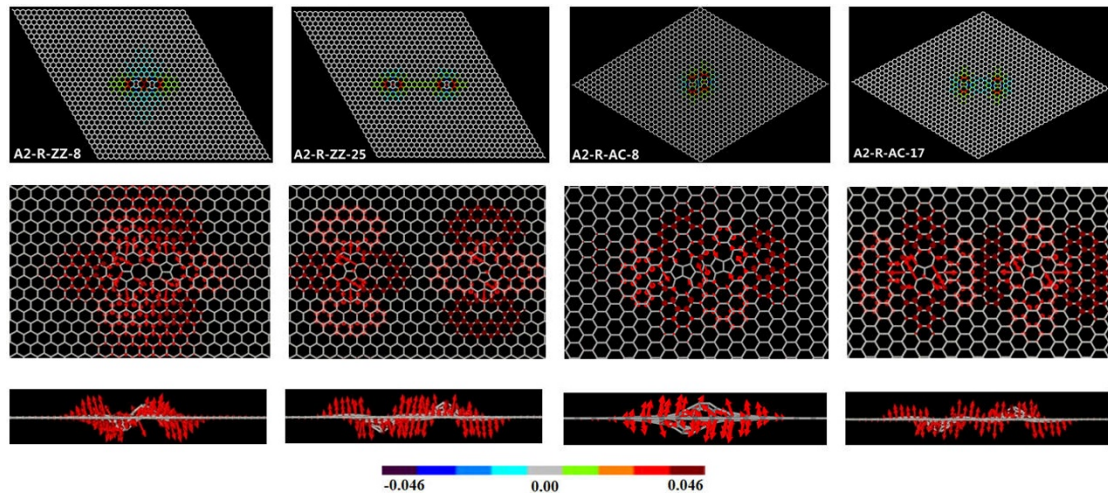


Figure 8. The interatomic bonds colored with stretched (red) or compressed (blue) and the displacements of the carbon atoms with red arrows of the two 7-55-7 pair (A_2) defects sites are reverse side along the glide ZZ and AC direction, respectively, according to the bond length distortion with respect to that of perfect graphene (1.42 \AA) induced by the defects pairs at different separation distances.

From Fig. 9 and Table 1, we can see that in $V_2(555-777)$ pair structure, the overall

bond length distortion $\Sigma(\Delta r)^2$ and bond angle distortion $\Sigma(\Delta\theta/\theta_0)^2$ along armchair direction is larger than the corresponding defects separated along the zig-zag direction. Opposite is true for $A_2(7-55-7)$ pairs either on the same side or different sides of graphene where the deformation is larger when the defect pair are separated along the zig-zag direction.

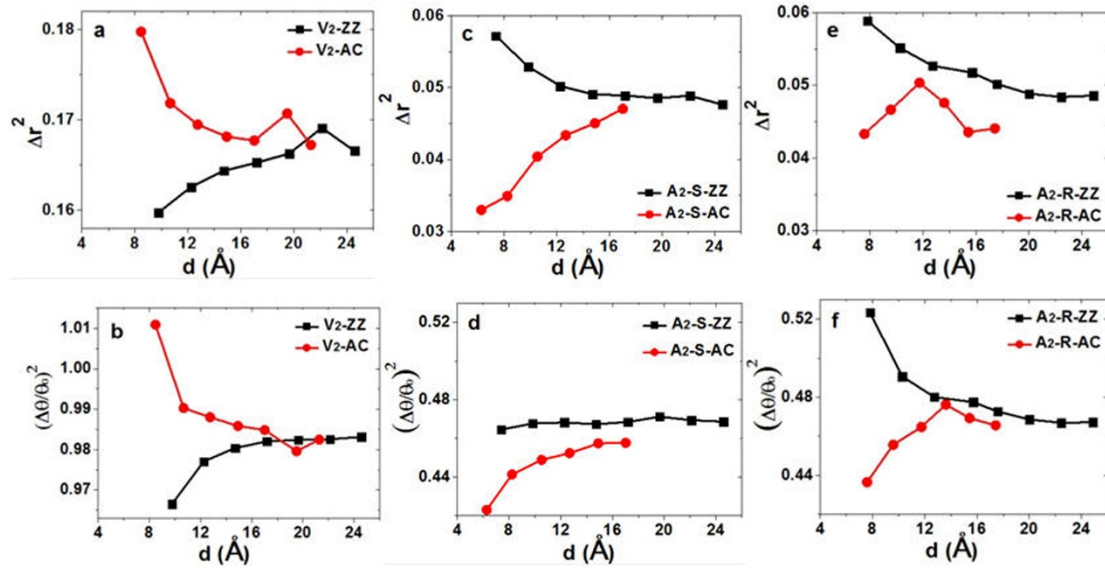


Figure 9. Bond length distortion and bond-angle distortions of the defected graphene with respect to those of perfect graphene as the function of the separation distance between the two defects along the glide ZZ and AC direction, respectively.

3.2.3. Defects interaction caused by the lattice distortion. In order to gain more detail insights into the defect interaction energy caused by the lattice distortion discussed above, we estimate the elastic energy caused by the defect pairs at different separation directions and distances based on the results of the lattice distortion discussed above,

$$E_d = \alpha \sum_{m=1}^{N_b} (\Delta r_m)^2 + \beta \sum_{n=1}^{N_a} \left(\frac{\Delta\theta_n}{\theta_0} \right)^2 \quad (2)$$

where Δr_m is the deviation of bond length from its equilibrium value in perfect graphene

and N_b is the total number of nearest neighbor bonds; $\Delta\theta_n$ is deviation of bond angle from the perfect bond-angle $\theta_0 (=120^\circ)$ in graphene and N_a is the total number of angles formed by nearest neighbor bonds. The coefficient α is the effective two-body force constant in graphene and β is related to the three-body force constant and measures the energy cost due to the bond angle distortions. The values of these two coefficients are 9.227 eV/\AA^2 and 11.594 eV respectively taken from the fitting to the formation energies of various single defects on graphene in our previous study.³⁶ The results of elastic energy E_d estimated from Eq. (2) for the three defect pairs are shown in the top panel of Fig. 10. These energy values are also listed in Table 1. The horizontal dashed lines in the Fig. 10 indicate the elastic energies of two isolated defects of each kind. Deviations from the dashed lines can be regarded as the elastic contribution to the interaction energies between the defect pairs on graphene.

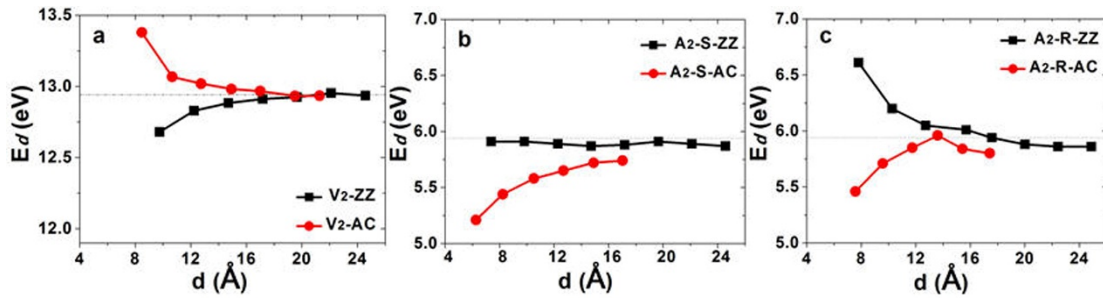


Figure 10. Elastic energy of the defect pairs on graphene calculated using Eq. (2). The horizontal dashed lines indicate the elastic energies of two isolated defects of each kind, respectively.

From Fig. 10 (a), we can see that for a $V_2(555-777)$ on graphene, there is an attractive elastic interaction between the defects when they separated along the zig-zag direction, while repulsive along the arm-chair direction. The contribution from the

elastic interactions accounts about two third of the total interaction energies, indicating the elastic interaction is dominate for the $V_2(555-777)$ pair on graphene. By contrast, there is an attractive elastic interactions for both $A_2-S(7-55-7)$ pair and $A_2-R(7-55-7)$ pair along the AC direction on graphene as one can see from Fig. 10 (b) and (c). While the elastic attraction for $A_2-R(7-55-7)$ pair along the AC direction can account for about 75% of total attractive interaction of the pair, it is intriguing to see the attractive elastic interaction for $A_2-S(7-55-7)$ pair along the AC direction is opposite to the total interaction which is strongly repulsive as shown in Fig. 5 (b). We will try to address this point in the next subsection. Finally, we note that for the A_2 pairs along the ZZ direction, there is almost no elastic interaction for $A_2-S(7-55-7)$ pair while there is a strong elastic repulsion for $A_2-R(7-55-7)$ pair which accounts for about 60% of the total repulsion.

3.4 Electron charge redistribution induced by the defects. From the analysis and discuss above, we see that elastic interactions contribute only a portion of total interactions of the defect pairs. The rest part of contributions can be regarded originating from electronic (including both electrostatic and dipole-dipole) interactions. Detail analysis of electronic interactions is not straightforward from our TB calculations. We therefore choose to study the electron charge redistribution caused by defect pairs. The electron charge on each atom is evaluated by Mulliken charge analysis based on the eigenvectors of the Hamiltonian matrix and the elements of the overlap matrix from our tight-binding calculations.³⁶ The results of charge difference between defected and perfect graphene are shown in Fig. 11. The deferential charge densities plotted in Fig.

11 are obtained by a Gaussian smearing factor of 0.001e on the Mulliken charge on each atom in defective and perfect graphene. Therefore, blue color indicates the loss of electrons and the red color indicates the gain of electrons on the carbon atoms induced by the defects. The charge varies from -0.1 to 0.2 e. It is also interesting to note that pentagon defects tend to gain more electrons while heptagons lose electrons on the defect pairs. We found the charge variation induced by the defects is well localized near the defect pairs, and decay rapidly away from the defects.

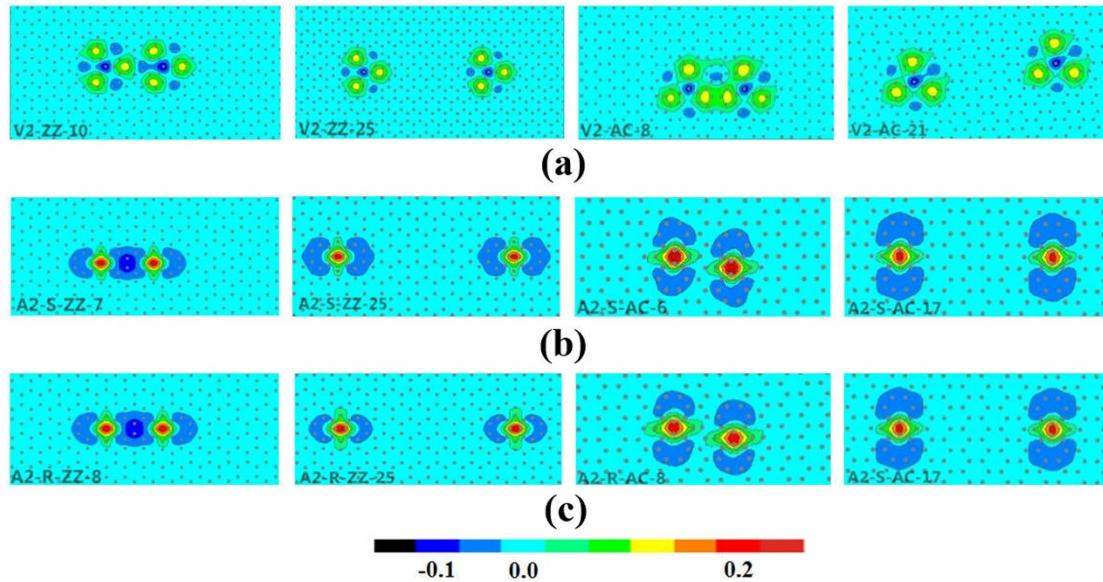


Figure 11. The difference of Mulliken charge on each atom in the defected graphene relative to that of perfect graphene along the glide ZZ and AC direction. The results are from TB calculation and analysis.

From Fig. 11 (a) we can see that the electron redistribution due to the defects are moderate for the $V_2(555-777)$ pair on graphene. These results suggest that the electric interaction energy would be moderate, consistent with the results that the defect interaction energies are dominated by the elastic interactions discussed above. By contrast, the change in the electron distribution caused by both $A_2-S(7-55-7)$ and A_2-

R(7-55-7) pairs are significant and well localized in the defect cores as one can see from Fig. 11 (b) and (c). The strong electron localization at the A_2 defect will cost a core energy of $1.682 \times 2.0 = 3.364$ eV for each isolated A_2 defect (or 6.728 eV for two A_2 defects) from our model in Ref. 36. It should be noted that this core energy, although quite large, does not affect the defect interaction energy. However, when two A_2 defects on the same side of graphene get close enough along the AC direction (i.e., A_2 -S(7-55-7) pair), the localized electrons on the two defects can be strongly overlapped and repulsive. This can explain why the total interaction between A_2 -S(7-55-7) pair is strongly repulsive although elastic interaction is attractive (see the subsection above). On the other hand, the excess electrons on the A_2 -S(7-55-7) pair along the ZZ direction can form bonds and provide attractive interaction between the two defect although there is no elastic interaction between them. In the case where two A_2 defects are on different sides of graphene (i.e., A_2 -R(7-55-7) pair), the characteristics of the interaction between the two A_2 defects are different from that of A_2 -S(7-55-7) pair due to the geometry difference, although the electron localization on each defect is similar to the case of A_2 -S(7-55-7).

To confirm the above picture inferred from the TB calculations, we also performed first-principles calculations to study the energy and electronic structures of the A_2 -S(7-55-7) pair and A_2 -R(7-55-7) pair separated along the AC direction by 6.27 Å and 7.80 Å, respectively. The numbers of atoms in the supercells were 292 and 452 for the A_2 -S(7-55-7) and A_2 -R(7-55-7) defect pairs, respectively. The atomic positions were relaxed until the force on each atom became less than 0.02 eV/Å. The calculations were

done using a slab geometry with sufficiently thick vacuum region ($\geq 10 \text{ \AA}$) to prevent the unwanted interaction between periodic images. $3 \times 3 \times 1$ k -point meshes are used. The DFT calculations show that the formation energy of the A_2 -S(7-55-7) defect pair is about 2.7 eV higher than that of the A_2 -R(7-55-7) defect pair, suggesting that there is more repulsion between the A_2 pair on the same side of the graphene compare to that of on different sides of graphene. This result is consistent with the prediction from the TB calculations discussed above. We also calculate the charge density difference (i.e., the difference between the self-consistent charge and the superposition of the atomic charge) to see the charge redistribution caused by the defect pairs. The results as plotted in Fig. 12 show that more charges are accumulated around the defects which is also consistent with the prediction from our TB calculations.

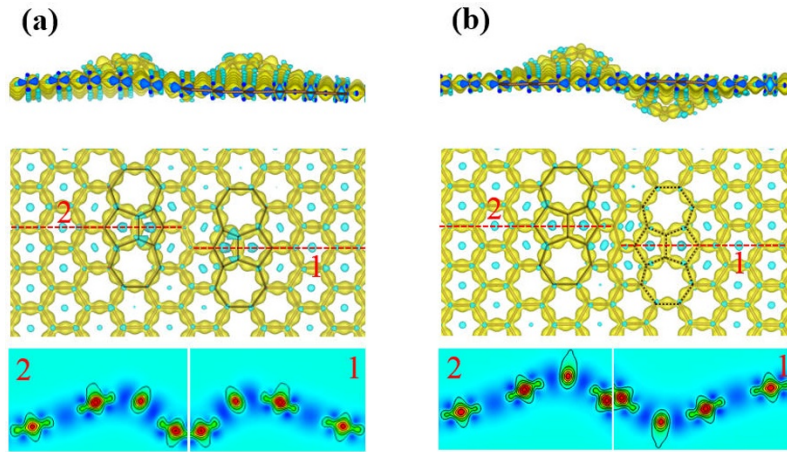


Figure 12. Differential charge density of (a) A_2 -S(7-55-7) and (b) A_2 -R(7-55-7) from first-principles DFT calculations. From the top to bottom panel is the 3D side-view, 3D top-view, and 2D-slice view respectively. The 3D views are plotted with charge contour value of $0.018 e/\text{bohr}^3$, and the color scale in the 2D-slice view is approximately $-0.03 \sim +0.08 e/\text{bohr}^3$.

4. CONCLUSIONS

In summary, we have studied the interaction energy, lattice distortions and electron

charge redistribution for reconstructed divacancy $V_2(555-777)$ pair and di-atom defect $A_2(7-55-7)$ pair separated along the glide zig-zag and armchair directions on graphene, respectively. We showed the V_2 pair is attractive along the ZZ direction while repulsive along the AC direction. About 2/3 of the total interaction energies can be attributed to the elastic interaction due to the graphene lattice distortion induced by the V_2 pair. For the A_2 pair, the characteristic of the interaction depends on whether the A_2 pair is on the same side of graphene or on the different sides of graphene. When the A_2 pair is on the same side of graphene (i.e., $A_2-S(7-55-7)$), the overall interaction along the AC direction is repulsive although the contribution from the elastic interaction is attractive. This strong repulsive interaction can be ascribed to electron repulsion from the localized electrons on the A_2 defect when the two A_2 defects get close enough along AC direction. When the two A_2 defects are located on different sides of graphene (i.e., $A_2-R(7-55-7)$ pair), the electronic interaction between the two A_2 defects is opposite to that of $A_2-S(7-55-7)$ pair. At the same time the electronic interaction strength is weaker, although the electron localization on each defect is similar to the case of $A_2-S(7-55-7)$.

■ AUTHOR INFORMATION

Corresponding Author

*E-mail: wangcz@ameslab.gov (CZ.W.); zhangw_bxx@jlu.edu.cn (W.Z.).

■ ACKNOWLEDGMENTS

W. Zhang acknowledges the support from The Education Department of Jilin Province and Science and Technology Plan (No. JJKH20180074KJ), and supported by the Natural Science Foundation of China (Grant Nos. 21873038 and 21573088). Work at Ames Laboratory was supported by the US Department of Energy, Office of Science, Basic Energy Sciences, Division of Materials Science and Engineering, including a grant of computer time at the National Energy Research Scientific Computing Centre (NERSC) in Berkeley, CA under Contract No. DE-AC02-07CH11358.

■ REFERENCES

(1) Qin, H. S.; Sun, Y.; Liu, J. Z.; Liu, Y. L. Mechanical Properties of Wrinkled Graphene Generated by Topological Defects. *Carbon* **2016**, *108*, 204-214.

(2) Bao, W. Z.; Miao, F.; Chen, Z.; Zhang, H.; Jang, W. Y.; Dames, C.; Lau, C. N. Controlled Ripple Texturing of Suspended Graphene and Ultrathin Graphite Membranes. *Nat. Nanotechnol* **2009**, *4*, 562-566.

(3) Ni, G. X.; Zheng, Y.; Bae, S.; Kim, H. R.; Pachoud, A.; Kim, Y. S.; Tan, C. L.; Im, D.; Ahn, J. H.; Hong, B. H.; Özyilmaz, B. Quasi-Periodic Nanoripples in Graphene Grown by Chemical Vapor Deposition and Its Impact on Charge Transport. *ACS Nano*, **2012**, *6*, 1158-1164.

(4) Lim, C. H. Y. X.; Sorkin, A.; Bao, Q.; Li, A.; Zhang, K.; Nesladek, M.; Loh, K. P. A Hydrothermal Anvil Made of Graphene Nanobubbles on Diamond. *Nat. Commun.*, **2013**, *4*, 1556.

(5) Levy, N.; Burke, S. A.; Meaker, K. L.; Panlasigui, M.; Zettl, A.; Guinea, F.; Castro Neto,

A. H.; Crommie, M. F. Strain-Induced Pseudo-Magnetic Fields Greater Than 300 Tesla in Graphene Nanobubbles. *Science*, **2010**, *329*, 544-547.

(6) Lu, J.; Castro Neto, A. H.; Loh, K. P. Transforming Moire Blisters into Geometric Graphene Nano-Bubbles. *Nat. Commun.*, **2012**, *3*, 823.

(7) Bahamon, D. A.; Qi, Z. N.; Park, H. S.; Pereira, V. M.; Campbell, D. K. Conductance Signatures of Electron Confinement Induced by Strained Nanobubbles in Graphene. *Nanoscale*, **2015**, *7*, 15300-15309.

(8) Khestanova, E.; Guinea, F.; Fumagalli, L.; Geim, A. K.; Grigorieva, I. V. Universal Shape and Pressure Inside Bubbles Appearing in Van Der Waals Heterostructures. *Nature Commun.*, **2016**, *7*, 12587.

(9) Ugeda, M. M.; Fernandez-Torre, D.; Brihuega, I.; Pou, P.; Martinez-Galera, A. J.; Perez, R.; Gomez-Rodriguez, J. M. Point Defects on Graphene on Metals. *Phys. Rev. Lett.*, **2011**, *107*, 116803.

(10) Banhart, F.; Kotakoski, J.; Krasheninnikov, A. V. Structural Defects in Graphene. *ACS Nano*, **2011**, *5*, 26-41.

(11) Lu, J.; Yeo, P. S. E.; Gan, C. K.; Wu, P.; Loh, K. P. Transforming C-60 Molecules into Graphene Quantum Dots. *Nat. Nanotechnol.*, **2011**, *6*, 247-252.

(12) Warner, J. H.; Fan, Y.; Robertson, A. W.; He, K.; Yoon, E.; Lee, G. D. Rippling Graphene at the Nanoscale through Dislocation Addition. *Nano Lett.*, **2013**, *13*, 4937-4944.

(13) Lehtinen, O.; Kurasch, S.; Krasheninnikov, A. V.; Kaiser, U. Atomic Scale Study of the Life Cycle of a Dislocation in Graphene from Birth to Annihilation. *Nat. Commun.*, **2013**, *4*, 2089.

- (14) Warner, J. H.; Margine, E. R.; Mukai, M.; Robertson, A. W.; Giustino, F.; Kirkland, A. I. Dislocation-Driven Deformations in Graphene *Science*, **2012**, *337*, 209-212.
- (15) Wang, L. P.; Fan, X. Q.; Li, W.; Li, H.; Zhu, M. H.; Pu, J. B.; Xue, Q. J. Space Irradiation-Induced Damage to Graphene Films. *Nanoscale*, **2017**, *9*, 13079.
- (16) Umoh, I. J.; Moktadir, Z.; Hang, S.; Kazmierski, T. J.; Mizuta, H. A Circuit Model for Defective Bilayer Graphene Transistors. *Solid-State Electron*, **2016**, *119*, 33-38.
- (17) Grantab, R.; Shenoy, V. B.; Ruoff, R. S. Anomalous Strength Characteristics of Tilt Grain Boundaries in Graphene. *Science*, **2010**, *330*, 946-948.
- (18) Gunlycke, D.; White, C. T. Graphene Valley Filter Using a Line Defect. *Phys. Rev. Lett.*, **2011**, *106*, 136806.
- (19) Carr, L. D.; Lusk, M. T. Defect Engineering Graphene Gets Designer Defects. *Nat. Nanotechnol*, **2010**, *5*, 316-317.
- (20) Yazyev, O. V.; Louie, S. G. Electronic Transport in Polycrystalline Graphene. *Nat. Mater.*, **2010**, *9*, 806-809.
- (21) Elias, D. C.; Nair, R. R.; Mohiuddin, T. M. G.; Morozov, S. V.; Blake, P.; Halsall, M. P.; Ferrari, A. C.; Boukhvalov, D. W.; Katsnelson, M. I.; Geim, A. K., et al. Control of Graphene's Properties by Reversible Hydrogenation: Evidence for Graphane. *Science*, **2009**, *323*, 610-613.
- (22) Lee, C.; Wei, X. D.; Kysar, J. W.; Hone, J. Measurement of the Elastic Properties and Intrinsic Strength of Monolayer Graphene. *Science*, **2008**, *321*, 385-388.
- (23) Li, M. Y.; Deng, T. Z. X.; Zheng, B.; Zhang, Y.; Liao, Y. G.; Zhou, H. M. Effect of Defects on the Mechanical and Thermal Properties of Graphene. *Nanomaterials*, **2019**, *9*, 347.
- (24) Novoselov, K. S.; Geim, A. K.; Morozov, S. V.; Jiang, D.; Zhang, Y.; Dubonos, S. V.;

Grigorieva, I. V.; Firsov, A. A. Electric Field Effect in Atomically Thin Carbon Films. *Science*, **2004**, *306*, 666-669.

(25) Mesáros, A.; Sadri, D.; Zaanen, J. Berry Phase of Dislocations in Graphene and Valley Conserving Decoherence. *Phys. Rev. B*, **2009**, *79*, 155111.

(26) Chen, J. H.; Li, L.; Cullen, W. G.; Williams, E. D.; Fuhrer, M. S. Tunable Kondo Effect in Graphene with Defects. *Nat. Phys.*, **2011**, *7*, 535.

(27) Nair, R. R.; Sepioni, M.; Tsai, I. L.; Lehtinen, O.; Keinonen, J.; Krasheninnikov, A.V.; Thomson, T.; Geim, A.K.; Grigorieva, I. V. Spin-Half Paramagnetism in Graphene Induced by Point Defects. *Nat. Phys.*, **2012**, *8*, 199-202.

(28) Levy, N.; Burke, S. A.; Meaker, K. L.; Panlasigui, M.; Zettl, A.; Guinea, F.; Castro Neto, A. H.; Crommie, M. F. Strain-Induced Pseudo-Magnetic Fields Greater Than 300 Tesla in Graphene Nanobubbles. *Science*, **2010**, *329*, 544-547.

(29) Carpio, A.; Bonilla, L. L. Periodized Discrete Elasticity Models for Defects in Graphene. *Phys. Rev. B*, **2008**, *78*, 085406.

(30) Chen, S.; Chrzan, D. C. Continuum Theory of Dislocations and Buckling in Graphene. *Phys. Rev. B*, **2011**, *84*, 214103.

(31) Grantab, R.; Shenoy, V. B.; Ruoff, R. S. Anomalous Strength Characteristics of Tilt Grain Boundaries in Graphene. *Science*, **2010**, *330*, 946-948.

(32) Chen, S.; Ertekin, E.; Chrzan, D. C. Plasticity in Carbon Nanotubes: Cooperative Conservative Dislocation Motion. *Phys. Rev. B*, **2010**, *81*, 155417.

(33) Nardelli, M. B.; Yakobson, B. I.; Bernholc, J. Brittle and Ductile Behavior in Carbon Nanotubes. *Phys. Rev. Lett.*, **1998**, *81*, 4656-4659.

(34) Lu, W. C.; Wang, C. Z.; Zhao, L. Z.; Qin, W.; Ho, K. M. Three-Center Tight-Binding Potential Model for C and Si. *Phys. Rev. B*, **2015**, *92*, 035206.

(35) Zhang, W.; Lu, W. C.; Zhang, H. X.; Ho, K. M.; Wang, C. Z. Tight-Binding Calculation Studies of Vacancy and Adatom Defects in Graphene. *J. Phys.: Condens. Matter*, **2016**, *28*, 115001.

(36) Zhang, W.; Lu, W. C.; Zhang, H. X.; Ho, K. M.; Wang, C. Z. Lattice Distortion and Electron Charge Redistribution Induced by Defects in Graphene. *Carbon*, **2016**, *110*, 330-335.

(37) Kresse, G.; Hafner, J. Ab Initio Molecular Dynamics for Liquid Metals. *Phys. Rev. B*, **1993**, *47*, 558.

(38) Kresse, G.; Furthmüller, J. Efficient Iterative Schemes for Ab Initio Total-Energy Calculations Using a Plane-Wave Basis Set. *Phys. Rev. B*, **1996**, *54*, 11169.

(39) Blöchl, P. E. Projector Augmented-Wave Method. *Phys. Rev. B*, **1994**, *50*, 17953.

(40) Perdew, J. P.; Burke, K.; Ernzerhof, M. Generalized Gradient Approximation Made Simple. *Phys. Rev. Lett.*, **1996**, *77*, 3865.

(41) Lee, G. D.; Wang, C. Z.; Yoon, E.; Hwang, N. M.; Kim, D. Y.; Ho, K. M. Diffusion, Coalescence, and Reconstruction of Vacancy Defects in Graphene Layers. *Phys. Rev. Lett.*, **2005**, *95*, 205501.

Table 1. The bond-length and bond-angle distortions ($\Sigma(\Delta r)^2$ and $\Sigma(\Delta\theta/\theta_0)^2$), as well as the elastic energy E_d as the function of the separation distance between the two defects for the three types of defect pairs. E_d are calculated using Eq. (2). The defect formation energies E_f using Eq (1) from the TB calculations are also shown for comparison.

	Distance(Å)	$\Sigma(\Delta r)^2(\text{Å}^2)$	$\Sigma(\Delta\theta/\theta_0)^2$	E_d (eV)	E_f (eV)
V ₂ -ZZ-1	9.76	0.160	0.967	12.68	13.56
V ₂ -ZZ-2	12.24	0.163	0.977	12.83	13.75
V ₂ -ZZ-3	14.71	0.164	0.980	12.88	13.93
V ₂ -ZZ-4	17.18	0.165	0.982	12.91	13.92
V ₂ -ZZ-5	19.65	0.166	0.982	12.92	13.96
V ₂ -ZZ-6	22.11	0.169	0.983	12.95	14.18
V ₂ -ZZ-7	24.58	0.167	0.983	12.94	14.00
V ₂ -AC-1	8.47	0.180	1.011	13.38	14.49
V ₂ -AC-2	10.67	0.172	0.990	13.07	14.08
V ₂ -AC-3	12.74	0.169	0.988	13.02	14.13
V ₂ -AC-4	14.93	0.168	0.986	12.98	14.01
V ₂ -AC-5	17.01	0.168	0.985	12.97	14.05
V ₂ -AC-6	19.50	0.171	0.980	12.93	14.20
V ₂ -AC-7	21.28	0.167	0.982	12.93	14.03

	Distance(Å)	$\Sigma(\Delta r)^2(\text{Å}^2)$	$\Sigma(\Delta\theta/\theta_0)^2$	E_d (eV)	E_f (eV)
A ₂ -S-ZZ-1	7.38	0.057	0.465	5.91	12.33
A ₂ -S-ZZ-2	9.82	0.053	0.468	5.91	12.68
A ₂ -S-ZZ-3	12.27	0.050	0.468	5.89	12.77
A ₂ -S-ZZ-4	14.72	0.049	0.467	5.87	12.77
A ₂ -S-ZZ-5	17.18	0.049	0.468	5.88	12.77
A ₂ -S-ZZ-6	19.65	0.049	0.471	5.91	12.84
A ₂ -S-ZZ-7	22.10	0.049	0.469	5.89	12.77
A ₂ -S-ZZ-8	24.54	0.048	0.469	5.87	12.82
A ₂ -S-AC-1	4.17	0.031	0.393	4.84	15.51
A ₂ -S-AC-2	6.27	0.033	0.423	5.21	14.03
A ₂ -S-AC-3	8.23	0.035	0.441	5.44	13.26
A ₂ -S-AC-4	10.52	0.040	0.449	5.58	12.85
A ₂ -S-AC-5	12.68	0.043	0.452	5.65	12.66
A ₂ -S-AC-6	14.90	0.045	0.457	5.72	12.59
A ₂ -S-AC-7	17.02	0.047	0.458	5.74	12.45

	Distance(Å)	$\Sigma(\Delta r)^2(\text{Å}^2)$	$\Sigma(\Delta\theta/\theta_0)^2$	E_d (eV)	E_f (eV)
A ₂ -R-ZZ-1	7.8	0.059	0.523	6.61	13.80
A ₂ -R-ZZ-2	10.27	0.055	0.491	6.20	13.27
A ₂ -R-ZZ-3	12.72	0.053	0.480	6.05	13.02
A ₂ -R-ZZ-4	15.7	0.0518	0.477	6.01	12.92
A ₂ -R-ZZ-5	17.59	0.050	0.473	5.94	12.84
A ₂ -R-ZZ-6	20.01	0.049	0.469	5.88	12.80
A ₂ -R-ZZ-7	22.44	0.048	0.467	5.86	12.76
A ₂ -R-ZZ-8	24.88	0.049	0.467	5.86	12.73
A ₂ -R-AC-1	5.46	0.044	0.427	5.36	12.51
A ₂ -R-AC-2	7.58	0.043	0.436	5.46	12.01
A ₂ -R-AC-3	9.58	0.047	0.456	5.71	12.20
A ₂ -R-AC-4	11.74	0.050	0.465	5.85	12.40
A ₂ -R-AC-5	13.61	0.048	0.476	5.96	12.81
A ₂ -R-AC-6	15.43	0.044	0.469	5.84	13.15
A ₂ -R-AC-7	17.43	0.044	0.466	5.80	13.04

TOC Graphic

